Published in final edited form as:
*NMR Biomed*. 2012 January ; 25(1): 113–122. doi:10.1002/nbm.1723.

# Lactate MRSI and DCE MRI As Surrogate Markers of Prostate Tumor Aggressiveness

**J. Yaligar**#[1], **S. B. Thakur**#[1,2], **L. Bokacheva**#[1], **S. Carlin**[1], **H. T. Thaler**[3], **A. Rizwan**[1], **M. E. Lupu**[1], **Y. Wang**[1], **C. C. Matei**[2], **K. L. Zakian**[1,2], and **J. A. Koutcher**[1,2,4]

[1]Department of Medical Physics, New York, NY, United States

[2]Department of Radiology, New York, NY, United States

[3]Department of Epidemiology and Biostatistics, New York, NY, United States

[4]Department of Medicine Memorial Sloan-Kettering Cancer Center, New York, NY, United States

# These authors contributed equally to this work.

## Abstract

Longitudinal studies of lactate MR spectroscopic imaging (MRSI) and dynamic contrast-enhanced MR imaging (DCE-MRI) were performed at 4.7 T in two prostate tumor models grown in rats, the Dunning R3327-AT (AT) and Dunning H (H), to determine the potential of lactate and the perfusion/permeability parameter $Ak_{ep}$ as markers of tumor aggressiveness. Subcutaneous AT (n = 12) and H (n = 6) tumors were studied at different volumes between 100 and 2900 mm$^3$ (Groups 1 to 5). Lactate concentration was determined from Selective Multiple Quantum Coherence (Sel-MQC) MRSI using phantom substitution method. Tumor enhancement after administration of Gd-DTPA was analyzed using the Brix-Hoffmann model and the $Ak_{ep}$ parameter was used as a measure of tumor perfusion/permeability. Lactate was not detected in the smallest AT tumors (Group 1; 100–270 mm$^3$). In larger AT tumors, lactate concentration increased from 2.8 ± 1.0 mM (Group 2; 290–700 mm$^3$) to 8.4 ± 2.9 mM (Group 3; 1000–1340 mm$^3$), 8.2 ± 2.2 mM (Group 4; 1380–1750 mm$^3$), and then decreased to 5.0 ± 1.7 mM (Group 5; 1900–2500 mm$^3$) and was consistently higher in the tumor core than in the rim. Lactate was not detected in any of the Dunning H tumors. The mean tumor $Ak_{ep}$ values decreased with increasing volume in both tumor types, but were significantly higher in H tumors. In AT tumors, the $Ak_{ep}$ values were significantly higher in the rim than in the core. Histological hypoxic and necrotic fractions in AT tumors increased with volume from 0% in Group 1 to about 20% and 30%, respectively, in Group 5. Minimal amounts of hypoxia and necrosis were found in H tumors of all sizes. Thus the presence of lactate and heterogeneous perfusion/permeability are signatures of aggressive, metabolically deprived Dunning R3327-AT tumor, but not the slow-growing Dunning H tumor.

## Keywords

Lactate; Dunning R3327 H; Dunning R3327-AT; Prostate; MR spectroscopic imaging; Sel-MQC; DCE-MRI; Immunohistochemistry

---

Corresponding Author: Jason A. Koutcher, MD, PhD Department of Medical Physics Memorial Sloan Kettering Cancer Center 1275 York Avenue New York, New York 10065 212-639-8834 koutchej@mskcc.org.

Parts of this work were presented at the 16th Annual Meeting of the International Society for Magnetic Resonance in Medicine, Toronto, ON, Canada; 3-9 May 2008.

# INTRODUCTION

Patients with identical pathological cancer diagnoses often have different clinical courses. This unexplained disparity is particularly true of prostate cancer, a disease which is usually indolent, yet sometimes follows an aggressive course. The difficulty in *a priori* differentiating patients with aggressive versus indolent prostate cancer is a major clinical problem and often leads to patients being overtreated (1,2). Nomograms based on clinical parameters, such as prostate-specific antigen (PSA) level, Gleason grade, disease stage, etc., are useful for predicting outcomes and selecting patients for watchful waiting (3,4), but are imperfect, and therefore more reliable biomarkers are necessary.

In addition to tumor variations across patients, among the cells of a single tumor there are metabolic, physiologic and genetic differences, which determine tumor aggressiveness and can cause treatment failure and metastases (5,6). Due to inadequate blood perfusion provided by the immature and dysfunctional tumor vasculature, some areas, especially in fast-growing tumors, become hypoxic. Hypoxia has been implicated as a cause of the preferential selection of cells with greater metastatic potential (7,8), tumor progression (9), and resistance to treatment (10,11). To adapt to hypoxia, tumor cells may switch from oxidative phosphorylation to anaerobic glycolysis, which terminates with the formation of lactate. Lactate has been recognized as a marker of a higher risk of metastases and poor prognosis in cervical cancer and head and neck tumors (12,13). Changes in lactate concentrations have also been suggested to be an early marker of response to treatment (14,15). Since tumors evolve with growth, noninvasive detection of lactate may be useful for determining the distribution of hypoxic cells, monitoring the changes in tumor metabolism and response to treatment.

MRI and magnetic resonance spectroscopic imaging (MRSI) provide means for probing the tumor vasculature and metabolism noninvasively. MRSI enables detecting lactate and estimating its concentration, and dynamic contrast-enhanced MRI (DCE-MRI) allows for visualization and quantitation of the tumor perfusion and permeability. Since measuring lactate *in vivo* remains challenging due to the relatively low lactate concentration and an overlap between the spectra of lactate and lipids, the majority of lactate MRSI measurements has been done in animal models. Terpstra et al. found that in C6 gliomas in rats, lactate concentration measured by single-voxel MRS did not correlate either with the tumor volume, glucose availability or with the tumor blood flow, assessed by deuterium oxide washout, and was constant above a certain perfusion threshold (4.7 mL/100g/min) (16). It was thus concluded that the lactate concentration is determined by the balance between the hemodynamic and substrate supply factors. However, these results describe the average values over the entire tumor and may be affected by the tumor heterogeneity.

Prostate tumor models are well suited for studying the spatial heterogeneity of tumor perfusion and metabolism with MRI/MRSI. The established and well characterized Dunning prostate tumor model system has been shown to be useful for development of new therapies and molecular characterization of tumor properties (17). This tumor system enables studies of tumor aggressiveness through the comparison of an aggressive, highly anaplastic Dunning R3327-AT tumor (doubling time, 3.3 days) with its parental Dunning 3327-H tumor, a well-differentiated, hormone responsive, slow-growing tumor with a doubling time of 12–20 days. The Dunning H tumor has higher partial oxygen pressure levels, three to four times lower histologically determined hypoxic fraction (18-20), and longer radiation-induced growth delays (21) than the AT tumor. In both cells lines the perfusion was shown to be heterogeneous across the tumor. In Dunning H tumors grown in rats, the blood flow measured using the microspheres method was found to be higher in the tumor periphery than in the center and decreased with increasing tumor weight (22). In Dunning R3327-AT tumors in mice, high uptake of fluorodeoxyglucose (FDG) was shown to correlate positively with histologically measured tumor hypoxia and negatively correlate with blood flow in the central regions of the tumor (23). However, detailed *in vivo* studies of perfusion and lactate in these tumor lines have not been performed.

In this study we compared the tumor lactate concentrations measured by MRSI and tumor contrast enhancement assessed by DCE-MRI in Dunning R3327-AT and Dunning H tumors as a function of tumor size and location within the tumor.

# METHODS

## Animal Models and Cell Culture

Animal studies were conducted in compliance with protocols approved by the Institutional Animal Care and Use Committee. Dunning R3327-AT cells were seeded in 75 $cm^2$ flask and grown in 20 mL Dulbecco's Modified Eagle's Medium (DMEM; Lonza, Walkersville, MD, USA) containing 4.5 g/L of glucose and L-glutamine, without sodium pyruvate and supplemented with fetal calf serum (FCS) (10%) and penicillin-streptomycin (1%). Cells were cultured under sterile conditions at 37°C in a 95% humidified air and 5% carbon dioxide atmosphere. Trypsin-EDTA solution (0.05% trypsin with 0.53 mM EDTA in Hank's balanced salt solution (HBSS), without calcium and magnesium salts) was used to separate the cells. Twenty two male Copenhagen rats (Charles River Laboratories, Wilmington, MA, USA) were implanted with $5\times10^6$ Dunning R3327-AT tumor cells subcutaneously in the thigh region. Dunning H tumor was generously provided by Dr. Susan Dalrymple and Dr. John Isaacs (Johns Hopkins School of Medicine, Baltimore, MD, USA) and tumors were grown by implanting cubic tissue sections 2 mm on the side subcutaneously in the thigh of six male Fischer-Copenhagen rats (Harlan Sprague Dawley Inc., Indianapolis, IN, USA). At the time of the tumor implantation, the rats in both groups weighed about 250 g each.

Tumor volumes were calculated using a hemiellipsoid formula: $V = (\pi/6)\times x\times y\times z$, where x, y and z are the length, width and height of the tumor, respectively, which were measured with calipers and corrected for the skin thickness of 1.3 mm (21).

After the tumors reached approximately 100–200 $mm^3$, rats bearing AT tumors (n = 12) and H tumors (n = 6) were studied longitudinally with MRI. Each rat was imaged at two to five time points after tumor implantation and sacrificed immediately after the last imaging session. Histological analyses of necrosis and hypoxia were performed in four large AT tumors ($V \sim 2000$ $mm^3$) harvested at the end of the longitudinal study. Four more rats with smaller AT tumors ($V \sim 120 – 1450$ $mm^3$) were studied by MRI at a single time point, sacrificed after imaging and analyzed histologically. The remaining six rats with AT tumors ($V \sim 600 – 1300$ $mm^3$) were sacrificed without undergoing MRI and used for measuring tumor necrosis. The necrotic area was measured in a total of fourteen AT tumors and hypoxia-sensitive staining was performed in eight AT tumors. Both necrotic and hypoxic fractions were measured in all six Dunning H tumors.

For each tumor line, experimental data were grouped by tumor volumes. Dunning R3327-AT tumors were stratified as follows: 100–270 $mm^3$ (Group 1), 290–700 $mm^3$ (Group 2), 1000–1340 $mm^3$ (Group 3), 1380–1750 $mm^3$ (Group 4) and 1900–2500 $mm^3$ (Group 5). Dunning H tumors were also split into five similar groups: 220–430 $mm^3$ (Group 1), 640–800 $mm^3$ (Group 2), 1360–1650 $mm^3$ (Group 3), 1800–2240 $mm^3$ (Group 4), and 2425–2860 $mm^3$ (Group 5).

## MRI Experiments

For MRI experiments, rats were anesthetized with isoflurane (1.0 – 2.5%) mixed with air. A 24 gauge, ¾ inch long catheter (Terumo Medical Corporation, Elkton, MD, USA) was inserted into the tail vein prior to placing the rat in the magnet. During imaging, respiration was monitored by a respiration monitoring pad under the rat's abdomen. Body temperature was monitored and maintained at 37°C by wrapping the animal in a blanket. Imaging was performed on a Bruker BioSpin 4.7 T animal scanner (Bruker; Billerica, MA, USA) with a 40 cm wide bore and maximum gradient strength of 40 Gauss/cm. An in-house-made two-turn solenoid (diameter, 25 mm) was used as a transmitter/receiver for all studies. The tumor was positioned in the center of the magnet with the help of three perpendicular scout images (repetition time, TR = 100 ms; echo time, TE = 5 ms; field of view, FOV = 150.0×150.0 $mm^2$; slice thickness, 5.0 mm). Using the scout images as a spatial reference, a sagittal $T_2$-weighted image through the center of the tumor was collected using the multi-slice multi-echo sequence (MSME) with the following parameters: TR = 3734 ms; TE = 30 ms; matrix, 128×128; FOV = 40.0×40.0 $mm^2$; one slice; slice thickness, 5.0 mm; echo train length, ETL = 8; number of excitations, NEX = 2.

**In vivo Lactate MR Spectroscopic Imaging—**Lactate MRSI was performed using the Selective Multiple Quantum Coherence (Sel-MQC) editing sequence (24) with frequency-selective 15 ms single-lobe sinc pulses. This sequence provides excellent lipid and water suppression, as shown previously (24,25). The selection of lactate signal was achieved by applying three magnetic field gradients with the same combination and duration as described in Refs. (24,26) and the amplitude of 24 Gauss/cm. Magnitude spectra were collected with 256 data points, spectral width of 2500 Hz, TR = 2000 ms, TE = 204 ms, and NEX = 8. Two-dimensional chemical shift imaging was performed in the location specified by the $T_2$-weighted image (FOV = 40.0×40.0 $mm^2$; one slice; slice thickness, 5.0 mm) and with 16×16 phase encoding matrix, which resulted in voxel volume of 2.5×2.5×5.0 $mm^3$ = 31.3 $mm^3$. The total MRSI acquisition time was 75 min. Flip angles were calibrated using a Gd-doped water phantom studied with a one-pulse sequence. Sufficiently long TR values (8.0 s) were used to ensure that the signal was fully relaxed. For the shaped pulses of fixed duration described above, the transmitter power level was varied to find the maximum and minimum intensity of the water peak corresponding to 90° and 180° flip angles, respectively. Fine adjustments of the transmit power were then introduced for each animal.

*In vivo* measurements of lactate $T_1$ were performed in R3327-AT tumors (n = 3; volume (mean ± standard error of the mean (SEM)), 1180 ± 150 $mm^3$) by introducing a nonselective 180° sinc pulse into the Sel-MQC sequence (26) with TR = 10 s at eleven different values of inversion recovery times TI = 10, 50, 100, 200, 500, 1000, 1500, 2000, 4000, 6000, and 10000 ms. The $T_1$ values were calculated by fitting the spectral peak integrals *S*(TI) with the following expression:

$$S(TI)=S_0\left(1-2\,exp\left(-TI/T_1\right)+exp\left(-TR/T_1\right)\right), \quad [1]$$

in which $T_1$ and the fully relaxed signal value $S_0$ were treated as free parameters. The nonlinear least-squares fitting implemented with Levenberg-Marquardt algorithm was performed in Matlab (Mathworks, Natick, MA, USA). $T_2$ values were measured using Sel-MQC sequence with an additional $CH_3$-selective 180° pulse and TE varying from 10 ms to 1000 ms and fitting the peak integrals S(TE) with a monoexponential decay curve (26).

For quantification of *in vivo* lactate concentration using the substitution method (27), a cylindrical phantom (volume, 9.1 $cm^3$) containing a solution of 30 mM lactate and 25 μM Gd-DTPA in water was scanned with the same parameters as the ones used for *in vivo* imaging.

**DCE MR Imaging—**Following the lactate MRSI study, DCE-MRI was performed. Sagittal multi-slice, $T_1$-weighted images were obtained using gradient echo fast imaging (GEFI) sequence with the following parameters: TR = 50 ms; TE = 3 ms; flip angle, FA = 30°; matrix, 128×128; FOV = 40.0×40.0 $mm^2$; 3 slices; slice thickness, 2.0 mm; slice gap, 0.2 mm; NEX = 2; temporal resolution, 12 s; 96 time points. After acquiring ten multi-slice images for measurements of the baseline signal, Gd-DTPA (0.2 mmol/kg; Magnevist, Berlex Laboratories Inc., Wayne, NJ, USA) was manually injected through the tail vein catheter and dynamic images were acquired for about 19 min.

## MR Data Analysis

**Quantification of Lactate Concentration—**The MRSI data were Fourier transformed and the two-dimensional array of lactate spectra was superimposed on the $T_2$-weighted image using the 3DiCSI software package (courtesy of Dr. Truman Brown, Columbia University, New York, NY, USA). Spectral filtering using Lorentzian filter (3 Hz) and Gaussian filter (4 Hz) was applied. The free induction decay data of the tumor voxels were exported in ASCII format and analyzed in the Java-based Magnetic Resonance User Interface (jMRUI) software package (28). The fitting of the lactate methyl resonance was performed in the time domain using AMARES (Advanced Method for Accurate, Robust and Efficient Spectral fitting). The phantom MRSI data were processed similarly.

The lactate concentration, *C*, was calculated by referencing to a phantom voxel at the same location as follows:

$$C=C_{ref}f_{CL}\frac{A}{A_{ref}}\frac{(1-exp\,(-TR/T_{1ref}))}{(1-exp\,(-TR/T_1))}exp\left(-TE\left[\frac{1}{T_{2ref}}-\frac{1}{T_2}\right]\right). \quad [2]$$

Here $C_{ref}$ is the concentration of lactate in the phantom; $A_{ref}$ and $A$ are the areas under the lactate peak in the spectra of the phantom and tumor, respectively; $T_{1ref}$ and $T_{2ref}$ are the relaxation times of lactate in the phantom and $T_1$ and $T_2$ are the lactate relaxation times *in vivo*, and $f_{CL}$ is the correction factor for the difference between the coil loading by the phantom and the tumor.

To evaluate the spatial distribution of lactate, the tumor was segmented into the rim and the core. The tumor rim was defined as a single layer of tumor voxels along the tumor boundary; all other tumor voxels were considered to be the core. Voxels along the outer edge of the tumor that contained air were excluded; voxels located along the boundary between the tumor and muscle were included if they contained at least 75% tumor tissue.

**Pharmacokinetic Modeling of DCE-MRI Data—**DCE-MRI data were analyzed using the simplified two-compartment pharmacokinetic model of Hoffmann *et al*. (29,30) based on the model by Brix *et al*. (31). The signal in every tumor voxel *S*(*t*) was normalized to the baseline signal $S_0$ and resulting signal enhancement Δ*S* was fitted with the following equation (30)

$$\Delta S=\frac{S\,(t)-S_0}{S_0}=Ak_{ep}\frac{\left(e^{-k_{ep}t}-e^{-k_{el}t}\right.}{k_{el}-k_{ep}} \quad [3]$$

where A is the maximum value that the enhancement would reach in the absence of contrast elimination and $k_{ep}$ is the rate of the efflux of contrast from the extracellular, extravascular space (EES) to plasma. The plasma concentration is assumed to decrease exponentially with the rate of $k_{el}$. The constant A is proportional to the fractional volume of the EES ($v_e$) (30). The product $Ak_{ep}$, which at $k_{ep}t<<1$ represents the initial upslope of enhancement, is proportional to $K^{trans}$. In the absence of an experimentally determined arterial input function, we used $Ak_{ep}$ as a measure of combined perfusion and permeability of the tumor tissue. Nonlinear least-squares fitting of enhancement in every voxel was performed using an in-house program written in IDL (ITT, Boulder, CO, USA). The voxel maps of $Ak_{ep}$ were segmented into the rim and the core using the segmentation masks from the lactate concentration maps of the same tumor.

## Histopathological Analysis

### Immunohistochemical Staining—Animals were euthanized using carbon dioxide inhalation. Tumors were excised, snap-frozen in isopentane/dry ice, embedded in cutting medium (OCT 4583, Sakura Finetek, Torrance, CA, USA) and sliced into 8 μm-thick contiguous frozen sections obtained using a cryostat microtome (Microm International GmbH, Walldorf, Germany). Sections were fixed in 4% paraformaldehyde solution for 10 min at room temperature then blocked in Superblock-PBS (Pierce Biotechnology Inc., Rockford, IL, USA) for 1 hr, followed by either hematoxylin/eosin (H&E) for determination of tumor necrosis or immunofluorescence staining for pimonidazole distribution. Pimonidazole staining was carried out as described previously (32). As a control for non-specific antibody binding, some sections were stained with non-specific mouse immunoglobulin G (IgG) conjugated to fluorescein isothiocyanate (FITC).

Images of pimonidazole-stained tumor sections were acquired at high magnification (×100) using an Olympus BX40 fluorescence microscope (Olympus America Inc., Melville, NY, USA) equipped with a motorized stage (Prior Scientific Instruments Ltd., Cambridge, UK) and an appropriate filter. The individually captured image frames were rendered into a montage of the entire tumor section using ImagePro software (Media Cybernetics Inc., Bethesda, MD, USA). Images of H&E stained sections were acquired in a similar manner using bright field illumination.

**Histological Data Analysis—**The fractional area of tumor necrosis was determined from digital images of H&E-stained whole-tumor sections using Adobe Photoshop 7.0 (Adobe Systems Inc., San Jose, CA, USA). The whole tumor and regions of necrosis were manually delineated and the necrotic fraction was calculated as the ratio of the necrotic area to the whole tumor area.

For determination of the pimonidazole binding fraction (hypoxic fraction), images of pimonidazole-stained sections were converted to binary form using a threshold determined from the immunofluorescence intensity measured in tumor sections stained with the control antibody. The same threshold was used to analyze all tumors. Hypoxic fraction was calculated as the fractional area with pimonidazole staining intensity greater than the threshold value. For each tumor, the necrotic and hypoxic fractions were determined for sections from at least two different locations and the results were averaged.

## Statistical Analysis

Lactate concentration in every voxel was recorded as a numerical value or zero, if the peak was not detected. The lactate concentration was expressed as the mean ± SEM over the voxels in the whole tumor, tumor rim and core.

The behavior of the lactate concentration versus volume was analyzed using a statistical model with the following assumptions: 1) the expected value of lactate concentration followed a quadratic function of tumor volume; 2) there was random variation among rats in the maximum lactate concentration and the volume at which the maximum is reached; 3) there was a proportional difference between the core and rim voxels; 4) within each region, the voxel lactate concentration followed a censored log-normal distribution. The lactate versus volume data were fitted with a parabola as the simplest non-monotonic function. Data censoring was applied to account for a large number of voxels in which lactate was not detected. In these voxels the lactate concentration was assumed to be below the minimum detected voxel value found in the entire dataset (2.3 mM). We applied a non-linear mixed effects statistical model implemented in Proc NLMixed (SAS v. 9, SAS Institute Inc., Cary, NC, USA). The analysis of $Ak_{ep}$ values did not require censoring, because there were very few voxels with zero $Ak_{ep}$ values.

The relationships between the mean lactate concentration, $Ak_{ep}$ values and the histologically measured necrotic and hypoxic fractions were studied using linear regression.

# RESULTS

## Measurements of Lactate Concentration and $Ak_{ep}$ values

Among the twelve rats with AT tumors that were studied longitudinally, two had no detectable lactate in any session and were excluded from analysis. Among the remaining rats with AT tumors, nine were imaged at four different time points and one at only two points after tumor implantation. In two imaging sessions DCE-MRI data were not available because of contrast injection failure. The four additional AT tumors each studied at a single time point were imaged successfully. In total, forty complete DCE-MRI/MRSI datasets were available in AT tumors and two datasets contained only MRSI data. In six Dunning H rats, twenty four MRI/MRSI datasets were acquired, with each rat imaged at three to five time points.

The tumor volume doubling time for the R3327-AT tumor was found to be (mean ± SEM) 3.3 ± 0.2 days, which is significantly shorter than the doubling time for the Dunning H tumor (22.8 ± 2.0 days, $p<0.001$), in agreement with previous studies (21).

Figure 1 demonstrates examples of the lactate spectra and the corresponding $T_2$-weighted images obtained in the AT and H tumors at two different sizes (Group 2 and Group 4). In AT tumors (Figs. 1A and 1B)), well defined lactate peaks were observed (Fig. 1C), especially in larger tumors, while in Dunning H tumors, lactate was not detected at any volume (Figs. 1D and 1E).

The lactate relaxation times in the phantom were found to be $T_{1ref} = 0.74$ s and $T_{2ref} = 0.36$ s. In vivo, the relaxation times (mean ± SEM) in R3327-AT tumors were $T_1 = 1.61 \pm 0.03$ s and $T_2 = 0.20 \pm 0.02$ s, in agreement with previous results (26).

The profile of lactate concentration versus volume for the rats with AT tumors varied among tumors (Fig. 2). In six tumors, the lactate concentration first increased, reached a maximum at the tumor volume of about 1000–1500 $mm^3$ and declined at higher volumes (Fig. 2, rats 3, 4, 6, 7, 8 and 10). In four other AT tumors, the lactate concentration increased with volume and/or reached a plateau within the studied volume range (rats 1, 2, 5 and 9). The presence of the maximum in lactate versus volume data was significant, as indicated by the significantly negative quadratic term in the statistical model fit ($p<0.001$).

Lactate was not detected in any of the AT tumors in Group 1 (Fig. 3A). In Group 2, lactate was detected in 64% of the tumors and in 41% of the voxels within these tumors. The majority of tumors in Group 3 (89%) contained lactate and had the largest fraction of lactate-containing voxels (57%). At higher volumes, in Group 4 all tumors showed detectable lactate, but the fraction of lactate-containing voxels dropped to 48%. In the largest tumors from Group 5, 75% of tumors and 38% of their voxels had lactate. The number of lactate-containing voxels was about twice higher in the core than in the rim.

For tumors grouped by volume, the mean lactate concentration in the whole tumor first increased with volume and reached a maximum for Group 3 (8.4 ± 2.9 mM) and Group 4 (8.2 ± 2.2 mM), but declined at higher volumes (Fig. 3B, Table 1). Similar behavior was found in the tumor rim and core, but for all volumes the lactate concentration in the core was significantly higher than in the rim ($p<0.001$).

The $Ak_{ep}$ values of AT tumors in the whole tumor, rim and core decreased with increasing tumor volume (Fig. 3C; Table 1). In the whole tumor, $Ak_{ep}$ declined from $1.6 \pm 0.5$ min$^{-1}$ in Group 1 to $0.3 \pm 0.1$ min$^{-1}$ in Group 5. For all groups, the $Ak_{ep}$ values in the rim were significantly higher than in the core ($p<0.001$).

In Dunning H tumors, lactate was not detected in any of the tumors, irrespective of their volume. The mean $Ak_{ep}$ value in the whole tumor was $1.2 \pm 0.1$ min$^{-1}$ in Group 1 and decreased to $0.5 \pm 0.1$ min$^{-1}$ for Group 5 (Fig. 4, Table 2). The $Ak_{ep}$ values in the rim and the core also decreased with tumor volume ($p<0.001$ for both), and there was a trend for the $Ak_{ep}$ values in the rim to be higher than in the core. The $Ak_{ep}$ values in Dunning H tumors were significantly higher than the R3327-AT tumors, as measured in the whole tumor, the rim and the core (all $p<0.001$).

### Correlation of MRI/MRSI with Histology and Immunohistochemistry

In AT tumors, necrosis was found in tumors from Groups 2 to 5 (Figs. 5A and 5D). The necrotic fraction increased significantly with increasing tumor volume ($R^2 = 0.81$, $p < 0.001$) (Fig. 6). In smaller tumors ($V < 1000$ mm$^3$), the necrotic fraction did not exceed 3%. When these tumors were excluded, the correlation coefficient between the necrotic fraction and volume increased to $R^2 = 0.90$ ($p < 0.001$). The fractional tumor area positive for the hypoxia tracer pimonidazole (Figs. 5B and 5E) also increased with tumor volume ($R^2 = 0.70$, $p = 0.01$) (Fig. 6).

For tumors studied with both MRSI and histology ($n = 8$), the lactate concentration correlated with necrotic fraction when all data points were included ($R^2 = 0.68$, $p = 0.012$) and when the smallest tumor without necrosis was excluded ($R^2 = 0.69$, $p = 0.020$). In the same tumors, the hypoxic fraction also showed a positive correlation with the lactate concentration when all data points were included ($R^2 = 0.67$, $p = 0.013$), although this correlation failed to reach significance when the tumor at the smallest volume and zero hypoxic fraction was excluded ($R^2 = 0.28$, $p = 0.220$).

In contrast, the Dunning H tumors had no observable necrosis and minimal pimonidazole positivity even at volumes approaching 2300 mm$^3$ (Figs. 5C and 5F).

## DISCUSSION

We have measured the lactate concentration and the perfusion/permeability parameter $Ak_{ep}$ in two different prostate tumor lines, the fast-growing Dunning R3327-AT and slow-growing Dunning H tumor. In the smallest AT tumors (Group 1, 100–270 mm$^3$), lactate is not detected and the $Ak_{ep}$ values are uniformly high throughout the tumors. This suggests that at this size tumors receive adequate delivery of oxygen and nutrients to meet their metabolic requirements. In the next volume group (Group 2, 290–650 mm$^3$) about two thirds of tumors contain lactate. In these tumors the contrast enhancement becomes spatially heterogeneous and shows a highly enhancing rim and a poorly enhancing core, in which the $Ak_{ep}$ values are two to three times lower than in the rim. The mean tumor $Ak_{ep}$ values in

Group 2 tumors drop to about a half of their values found in Group 1. The onset of heterogeneity of the perfusion/permeability in AT tumors and the concomitant appearance of lactate may indicate that the tumor has evolved into a metabolically deprived state. As the tumors continue to grow, the $Ak_{ep}$ gradually decreases, while the concentration of lactate increases and reaches a maximum for tumors in Groups 3 and 4 (1000 – 1750 $mm^3$) (Figs. 3B and 3C). The increase of the lactate concentration is accompanied by the growth of hypoxic fraction from zero in the smallest tumors to about 20% in tumors reaching 1500 $mm^3$ volume. Necrotic fraction remains small (below 3%) in tumors up to 1000 $mm^3$ and grows with volume above this threshold. In tumors larger than 1500 $mm^3$, the lactate concentration decreases, while the necrotic and hypoxic fractions continue to increase and reach 20% and 30%, respectively, in the largest AT tumors (Fig. 6). These observations are consistent with the hypothesis that in the state of perfusion and metabolic deficits, the tumor increasingly relies on anaerobic glycolysis, which results in formation and accumulation of lactate.

In contrast, in the Dunning H tumors, lactate is not detected at any tumor volume. The $Ak_{ep}$ values decrease with increasing tumor volume, but do not show an abrupt drop, as observed when the rim and core form in AT tumors. In contrast to the AT tumors, the largest decrease of $Ak_{ep}$ in Dunning H tumors occurs between the largest volume groups (Groups 4 and 5). The $Ak_{ep}$ in the core is still lower than in the rim, but only by about 20-25% of the rim value. This indicates that in Dunning H tumors perfusion/permeability is more uniform across the tumor than in AT tumors (Fig. 4, Table 2). Overall, the $Ak_{ep}$ values in Dunning H tumors are higher than those in R3327-AT tumors. In agreement with previous studies (20), the histopathological analysis and pimonidazole staining of Dunning H tumors show minimal necrosis and hypoxia, which develop mainly in the largest tumors. The absence of lactate, hypoxia and necrosis in the Dunning H tumors indicates that these tumors do not develop a metabolically deprived state. Because of its lower growth rate, Dunning H tumor has lower energy demands, and the tumor vasculature is better able to keep up with the tumor's metabolic requirements. This is consistent with the higher and more uniform perfusion/permeability found in H tumors compared to the AT tumors. The contrasting behavior of the AT and H tumors suggests that the presence of lactate is a feature of an aggressive, heterogeneously vascularized and metabolically stressed tumor, but not of the slow-growing and relatively uniformly vascularized tumor.

One of the difficulties of comparing lactate and perfusion/permeability measurements lies in the difference between the spatial resolutions of the two datasets. The voxel size of MRSI is large compared to the MRI voxel. Thus when the tumor is segmented into the rim and core, we can expect that many voxels will contain heterogeneous tissue with varied perfusion/permeability and metabolic properties, although this partial volume effect should decrease for larger tumors. Tumor segmentation into rim and core can be done using various criteria. We defined the rim as a single layer of MRSI voxels along the border of the tumor and therefore, due to the large size of MRSI voxels, some of the rim voxels contain core tissue. It is therefore possible that the observation of a maximum of lactate concentration in the rim at intermediate tumor volumes is a result of this partial volume effect and the true lactate concentration in the rim remains stable across all tumor volumes.

Tumors have high lactate levels, due to increased production and/or decreased clearance of lactate. We hypothesize that lactate is a potential marker of prostate tumor aggressiveness. Lactate concentrations have been shown to have prognostic value in other tumors (12,13,33,34) and have correlated with a high probability of metastasis and decreased patient survival. Based on the heterogeneity of tumor lactate concentration, hypothetically the areas of aggressive, hypoxic tumors could be delineated for localized therapy or biopsy.

Previous *ex vivo* studies have indicated that lactate is elevated in prostate cancer (35-37), although such studies are subject to errors, because lactate concentration increases with tissue death after surgery. The conversion rates of pyruvate to lactate have been investigated using hyperpolarized $^{13}$C spectroscopic imaging. Chen *et al.* (38) studied the transgenic adenocarcinoma of mouse prostate (TRAMP) and found that after infusion of $^{13}$C-labeled pyruvate, lactate synthesis could be detected in both primary and metastatic prostate tumors. Albers *et al*. (39) found that after the injection of $^{13}$C pyruvate, the lactate levels were about twice as high in high grade tumors than in low grade TRAMP tumors, where tumor grade was assessed by a histological index introduced by the authors. Our study also indicates that lactate is present in the tumor with a more aggressive phenotype, as measured by growth rate, as the tumor develops hypoxia. Numerous recent studies have shown that tumor hypoxia and altered metabolism are interconnected. Hypoxia is known to enhance glycolytic activity and likely works via the HIF1-α pathway. Monitoring lactate concentrations *in vivo* could be used to evaluate the activity and determine an appropriate dose of targeted drugs aimed at inhibiting various metabolic pathways.

Prostate cancer is an important tumor to study because of its high incidence and difficulty predicting its clinical course. The Dunning tumor models have been used extensively to evaluate novel therapies, some of which have subsequently been moved to the clinic including hormonal therapy (40-43), chemotherapy (44), radiation (21,44), gene therapy (45), and other innovative treatments (46,47). The Dunning tumor lines have many similar characteristics to human clinical prostate cancer (48,49), but are syngeneic to the rat. This enables one to avoid issues associated with xenograft models, which initially have a murine vascular system. Although the R3327-AT tumor has significant necrosis (15-20% of the total tumor volume at volumes of 2000-2500 mm$^3$), which is not commonly seen in human tumors, reports of prostate tumor necrosis in patients, particularly in aggressive tumors, have been published (50,51). While all tumor models are imperfect, the choice of these tumor models for investigating contrasting tumor properties is reasonable. Further studies with an orthotopic model are feasible and will require further optimization of lactate detection methods (25).

## CONCLUSION

Lactate is detected in a heterogeneous pattern in the fast-growing R3327-AT tumor, but is not detected in the slowly growing Dunning H, which suggests that the presence of lactate may be a feature of aggressive tumors. The core of the AT tumor is prone to accumulate more lactate than the rim of the tumor, probably because the core has a poorer oxygen and blood supply. This observation is supported by the perfusion/permeability measures derived from DCE-MRI data, which are significantly lower in the core than in the rim.

## Acknowledgments

The authors gratefully acknowledge support from P01 CA115675, P50-CA92629, P50 CA86438, PC041115, and DOD W81XWH-09-1-0042. The authors are grateful to Dr. John Isaacs and Dr. Susan Dalrymple at Johns Hopkins School of Medicine for providing the Dunning H tumor.

## Abbreviations

| | |
|---|---|
| **PSA** | prostate-specific antigen |
| **MRSI** | magnetic resonance spectroscopic imaging |
| **DCE-MRI** | dynamic contrast-enhanced MRI |

| | |
|---|---|
| **AT** | Dunning R3327-AT tumor |
| **H** | Dunning R3327-H tumor |
| **MSME** | multi-slice multi-echo [MR sequence] |
| **GEFI** | gradient echo fast imaging [MR sequence] |
| **Sel-MQC** | Selective Multiple Quantum Coherence [sequence] |
| **SEM** | standard error of the mean |
| **EES** | extracellular extravascular space |
| **AMARES** | Advanced Method for Accurate, Robust and Efficient Spectral fitting |
| **FDG** | fluorodeoxyglucose |
| **DMEM** | Dulbecco's modified Eagle's medium |
| **HBSS** | Hank's balanced salt solution |
| **H&E** | hematoxylin and eosin |
| **FCS** | fetal calf serum |
| **IgG** | immunoglobulin |
| **FITC** | fluorescein isothiocyanate |

## REFERENCES

1. Miller DC, Gruber SB, Hollenbeck BK, Montie JE, Wei JT. Incidence of initial local therapy among men with lower-risk prostate cancer in the United States. J Natl Cancer Inst. 2006; 98:1134–1141. [PubMed: 16912266]
2. Cooperberg MR, Lubeck DP, Meng MV, Mehta SS, Carroll PR. The changing face of low-risk prostate cancer: trends in clinical presentation and primary management. J Clin Oncol. 2004; 22:2141–2149. [PubMed: 15169800]
3. Chun FK, Karakiewicz PI, Huland H, Graefen M. Role of nomograms for prostate cancer in 2007. World J Urol. 2007; 25:131–142. [PubMed: 17333203]
4. Steyerberg EW, Roobol MJ, Kattan MW, van der Kwast TH, de Koning HJ, Schroder FH. Prediction of indolent prostate cancer: validation and updating of a prognostic nomogram. J Urol. 2007; 177:107–112. [PubMed: 17162015]
5. Nowell PC. The clonal evolution of tumor cell populations. Science. 1976; 194:23–28. [PubMed: 959840]
6. Gao C, Furge K, Koeman J, Dykema K, Su Y, Cutler ML, Werts A, Haak P, Vande Woude GF. Chromosome instability, chromosome transcriptome, and clonal evolution of tumor cell populations. Proc Natl Acad Sci U S A. 2007; 104:8995–9000. [PubMed: 17517657]
7. Lang GA, Iwakuma T, Suh YA, Liu G, Rao VA, Parant JM, Valentin-Vega YA, Terzian T, Caldwell LC, Strong LC, El-Naggar AK, Lozano G. Gain of function of a p53 hot spot mutation in a mouse model of Li-Fraumeni syndrome. Cell. 2004; 119:861–872. [PubMed: 15607981]
8. Perryman LA, Blair JM, Kingsley EA, Szymanska B, Ow KT, Wen VW, MacKenzie KL, Vermeulen PB, Jackson P, Russell PJ. Over-expression of p53 mutants in LNCaP cells alters tumor growth and angiogenesis in vivo. Biochem Biophys Res Commun. 2006; 345:1207–1214. [PubMed: 16723121]
9. Okawa T, Michaylira CZ, Kalabis J, Stairs DB, Nakagawa H, Andl CD, Johnstone CN, Klein-Szanto AJ, El-Deiry WS, Cukierman E, Herlyn M, Rustgi AK. The functional interplay between EGFR overexpression, hTERT activation, and p53 mutation in esophageal epithelial cells with activation of stromal fibroblasts induces tumor development, invasion, and differentiation. Genes Dev. 2007; 21:2788–2803. [PubMed: 17974918]

10. Lowe SW, Ruley HE, Jacks T, Housman DE. p53-dependent apoptosis modulates the cytotoxicity of anticancer agents. Cell. 1993; 74:957–967. [PubMed: 8402885]
11. Li G, Bush JA, Ho VC. p53-dependent apoptosis in melanoma cells after treatment with camptothecin. J Invest Dermatol. 2000; 114:514–519. [PubMed: 10692111]
12. Walenta S, Wetterling M, Lehrke M, Schwickert G, Sundfor K, Rofstad EK, Mueller-Klieser W. High lactate levels predict likelihood of metastases, tumor recurrence, and restricted patient survival in human cervical cancers. Cancer Res. 2000; 60:916–921. [PubMed: 10706105]
13. Walenta S, Salameh A, Lyng H, Evensen JF, Mitze M, Rofstad EK, Mueller-Klieser W. Correlation of high lactate levels in head and neck tumors with incidence of metastasis. Am J Pathol. 1997; 150:409–415. [PubMed: 9033256]
14. Bhujwalla ZM, Glickson JD. Detection of tumor response to radiation therapy by in vivo proton MR spectroscopy. Int J Radiat Oncol Biol Phys. 1996; 36:635–639. [PubMed: 8948348]
15. Aboagye EO, Bhujwalla ZM, Shungu DC, Glickson JD. Detection of tumor response to chemotherapy by 1H nuclear magnetic resonance spectroscopy: effect of 5-fluorouracil on lactate levels in radiation-induced fibrosarcoma 1 tumors. Cancer Res. 1998; 58:1063–1067. [PubMed: 9500472]
16. Terpstra M, High WB, Luo Y, de Graaf RA, Merkle H, Garwood M. Relationships among lactate concentration, blood flow and histopathologic profiles in rat C6 glioma. NMR Biomed. 1996; 9:185–194. [PubMed: 9067999]
17. Tennant TR, Kim H, Sokoloff M, Rinker-Schaeffer CW. The Dunning model. Prostate. 2000; 43:295–302. [PubMed: 10861749]
18. Yeh KA, Biade S, Lanciano RM, Brown DQ, Fenning MC, Babb JS, Hanks GE, Chapman DC. Polarographic needle electrode measurements of oxygen in rat prostate carcinomas: accuracy and reproducibility. Int J Radiat Oncol Biol Phys. 1995; 33:111–118. [PubMed: 7642408]
19. Zhao D, Constantinescu A, Chang CH, Hahn EW, Mason RP. Correlation of tumor oxygen dynamics with radiation response of the dunning prostate R3327-HI tumor. Radiat Res. 2003; 159:621–631. [PubMed: 12710873]
20. Zhao D, Ran S, Constantinescu A, Hahn EW, Mason RP. Tumor oxygen dynamics: correlation of in vivo MRI with histological findings. Neoplasia. 2003; 5:308–318. [PubMed: 14511402]
21. Thorndyke C, Meeker BE, Thomas G, Lakey WH, McPhee MS, Chapman JD. The radiation sensitivities of R3327-H and R3327-AT rat prostate adenocarcinomas. J Urol. 1985; 134:191–198. [PubMed: 4009821]
22. Daehlin L, Damber JE. Blood flow in the Dunning R3327H rat prostatic adenocarcinoma; effects of oestradiol and testosterone. Urol Res. 1986; 14:113–117. [PubMed: 3727214]
23. Pugachev A, Ruan S, Carlin S, Larson SM, Campa J, Ling CC, Humm JL. Dependence of FDG uptake on tumor microenvironment. Int J Radiat Oncol Biol Phys. 2005; 62:545–553. [PubMed: 15890599]
24. He Q, Shungu DC, van Zijl PC, Bhujwalla ZM, Glickson JD. Single-scan in vivo lactate editing with complete lipid and water suppression by selective multiple-quantum-coherence transfer (Sel-MQC) with application to tumors. J Magn Reson B. 1995; 106:203–211. [PubMed: 7719620]
25. Thakur SB, Yaligar J, Koutcher JA. In vivo lactate signal enhancement using binomial spectral-selective pulses in selective MQ coherence (SS-SelMQC) spectroscopy. Magn Reson Med. 2009; 62:591–598. [PubMed: 19526486]
26. Muruganandham M, Koutcher JA, Pizzorno G, He Q. In vivo tumor lactate relaxation measurements by selective multiple-quantum-coherence (Sel-MQC) transfer. Magn Reson Med. 2004; 52:902–906. [PubMed: 15389963]
27. Danielsen ER, Michaelis T, Ross BD. Three methods of calibration in quantitative proton MR spectroscopy. J Magn Reson B. 1995; 106:287–291. [PubMed: 7719627]
28. Naressi A, Couturier C, Castang I, de Beer R, Graveron-Demilly D. Java-based graphical user interface for MRUI, a software package for quantitation of in vivo/medical magnetic resonance spectroscopy signals. Comput Biol Med. 2001; 31:269–286. [PubMed: 11334636]
29. Hoffmann U, Brix G, Knopp MV, Hess T, Lorenz WJ. Pharmacokinetic mapping of the breast: a new method for dynamic MR mammography. Magn Reson Med. 1995; 33:506–514. [PubMed: 7776881]

30. Tofts PS. Modeling tracer kinetics in dynamic Gd-DTPA MR imaging. J Magn Reson Imaging. 1997; 7:91–101. [PubMed: 9039598]
31. Brix G, Semmler W, Port R, Schad LR, Layer G, Lorenz WJ. Pharmacokinetic parameters in CNS Gd-DTPA enhanced MR imaging. J Comput Assist Tomogr. 1991; 15:621–628. [PubMed: 2061479]
32. Cho H, Ackerstaff E, Carlin S, Lupu ME, Wang Y, Rizwan A, O'Donoghue J, Ling CC, Humm JL, Zanzonico PB, Koutcher JA. Noninvasive multimodality imaging of the tumor microenvironment: registered dynamic magnetic resonance imaging and positron emission tomography studies of a preclinical tumor model of tumor hypoxia. Neoplasia. 2009; 11:247–259. [PubMed: 19242606]
33. Brizel DM, Schroeder T, Scher RL, Walenta S, Clough RW, Dewhirst MW, Mueller-Klieser W. Elevated tumor lactate concentrations predict for an increased risk of metastases in head-and-neck cancer. Int J Radiat Oncol Biol Phys. 2001; 51:349–353. [PubMed: 11567808]
34. Walenta S, Chau TV, Schroeder T, Lehr HA, Kunz-Schughart LA, Fuerst A, Mueller-Klieser W. Metabolic classification of human rectal adenocarcinomas: a novel guideline for clinical oncologists? J Cancer Res Clin Oncol. 2003; 129:321–326. [PubMed: 12827509]
35. Cornel EB, Smits GA, Oosterhof GO, Karthaus HF, Deburyne FM, Schalken JA, Heerschap A. Characterization of human prostate cancer, benign prostatic hyperplasia and normal prostate by in vitro 1H and 31P magnetic resonance spectroscopy. J Urol. 1993; 150:2019–2024. [PubMed: 7693985]
36. Swanson MG, Zektzer AS, Tabatabai ZL, Simko J, Jarso S, Keshari KR, Schmitt L, Carroll PR, Shinohara K, Vigneron DB, Kurhanewicz J. Quantitative analysis of prostate metabolites using 1H HR-MAS spectroscopy. Magn Reson Med. 2006; 55:1257–1264. [PubMed: 16685733]
37. Tessem MB, Swanson MG, Keshari KR, Albers MJ, Joun D, Tabatabai ZL, Simko JP, Shinohara K, Nelson SJ, Vigneron DB, Gribbestad IS, Kurhanewicz J. Evaluation of lactate and alanine as metabolic biomarkers of prostate cancer using 1H HR-MAS spectroscopy of biopsy tissues. Magn Reson Med. 2008; 60:510–516. [PubMed: 18727052]
38. Chen AP, Albers MJ, Cunningham CH, Kohler SJ, Yen YF, Hurd RE, Tropp J, Bok R, Pauly JM, Nelson SJ, Kurhanewicz J, Vigneron DB. Hyperpolarized C-13 spectroscopic imaging of the TRAMP mouse at 3T-initial experience. Magn Reson Med. 2007; 58:1099–1106. [PubMed: 17969006]
39. Albers MJ, Bok R, Chen AP, Cunningham CH, Zierhut ML, Zhang VY, Kohler SJ, Tropp J, Hurd RE, Yen YF, Nelson SJ, Vigneron DB, Kurhanewicz J. Hyperpolarized 13C lactate, pyruvate, and alanine: noninvasive biomarkers for prostate cancer detection and grading. Cancer Res. 2008; 68:8607–8615. [PubMed: 18922937]
40. Schally AV, Redding TW, Comaru-Schally AM. Inhibition of prostate tumors by agonistic and antagonistic analogs of LH-RH. Prostate. 1983; 4:545–552. [PubMed: 6226942]
41. Isaacs JT, Coffey DS. Adaptation versus selection as the mechanism responsible for the relapse of prostatic cancer to androgen ablation therapy as studied in the Dunning R-3327-H adenocarcinoma. Cancer Res. 1981; 41:5070–5075. [PubMed: 7307008]
42. Redding TW, Schally AV. Inhibition of prostate tumor growth in two rat models by chronic administration of D-Trp6 analogue of luteinizing hormone-releasing hormone. Proc Natl Acad Sci U S A. 1981; 78:6509–6512. [PubMed: 6458815]
43. Redding TW, Schally AV. Inhibition of prostate tumor growth in two rat models by chronic administration of D-Trp6 analogue of luteinizing hormone-releasing hormone. Proc Natl Acad Sci USA. 1981; 78:6509–6512. [PubMed: 6458815]
44. Mador D, Ritchie B, Meeker B, Moore R, Elliott FG, McPhee MS, Chapman JD, Lakey WH. Response of the Dunning R3327H prostatic adenocarcinoma to radiation and various chemotherapeutic drugs. Cancer Treat Rep. 1982; 66:1837–1843. [PubMed: 6889915]
45. Sanda MG, Ayyagari SR, Jaffee EM, Epstein JI, Clift SL, Cohen LK, Dranoff G, Pardoll DM, Mulligan RC, Simons JW. Demonstration of a rational strategy for human prostate cancer gene therapy. J Urol. 1994; 151:622–628. [PubMed: 8308972]
46. Loening SA, Bonney WW, Fallon B, Gerber WL, Hawtrey CE, Lubaroff DM, Narayana AS, Culp DA. Cryotherapy. Prostate. 1984; 5:199–204. [PubMed: 6709521]

47. Tiwari RK, Geliebter J, Garikapaty VP, Yedavelli SP, Chen S, Mittelman A. Anti-tumor effects of PC-SPES, an herbal formulation in prostate cancer. Int J Oncol. 1999; 14:713–719. [PubMed: 10087319]

48. Hall M, Silverman L, Wenger AS, Mickey DD. Oncodevelopmental enzymes of the Dunning rat prostatic adenocarcinoma. Cancer research. 1985; 45:4053–4059. [PubMed: 2992772]

49. Lubaroff DM, Culp DA. Experience with an animal model for the study of prostatic carcinoma. Trans Am Assoc Genitourin Surg. 1977; 69:72–77. [PubMed: 617916]

50. Wang W, Epstein JI. Small cell carcinoma of the prostate. A morphologic and immunohistochemical study of 95 cases. Am J Surg Pathol. 2008; 32:65–71. [PubMed: 18162772]

51. Cai G, Ramdall RB, Levine P, Yang GC. Fine-needle aspiration of metastatic prostatic neuroendocrine carcinomas: cytomorphologic and immunophenotypic features. Diagn Cytopathol. 2008; 36:545–549. [PubMed: 18618716]

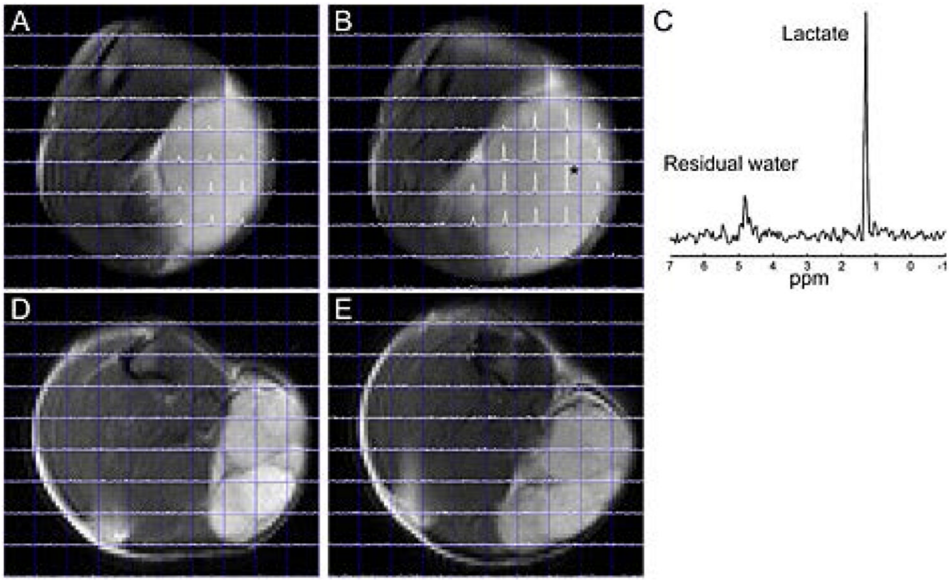

**Figure 1.**

Lactate spectra superimposed on T2-weighted images in R3327-AT and Dunning H tumors. The lactate spectra in the AT tumor imaged at V = 296 $mm^3$ (A) and V = 1455 $mm^3$ (B) show well-defined lactate peaks. The spectrum of the voxel in panel (B) marked with an asterisk is shown in panel (C). In contrast, the Dunning H tumor imaged at V = 227 $mm^3$ (D) and V = 1364 $mm^3$ (E) shows no lactate.

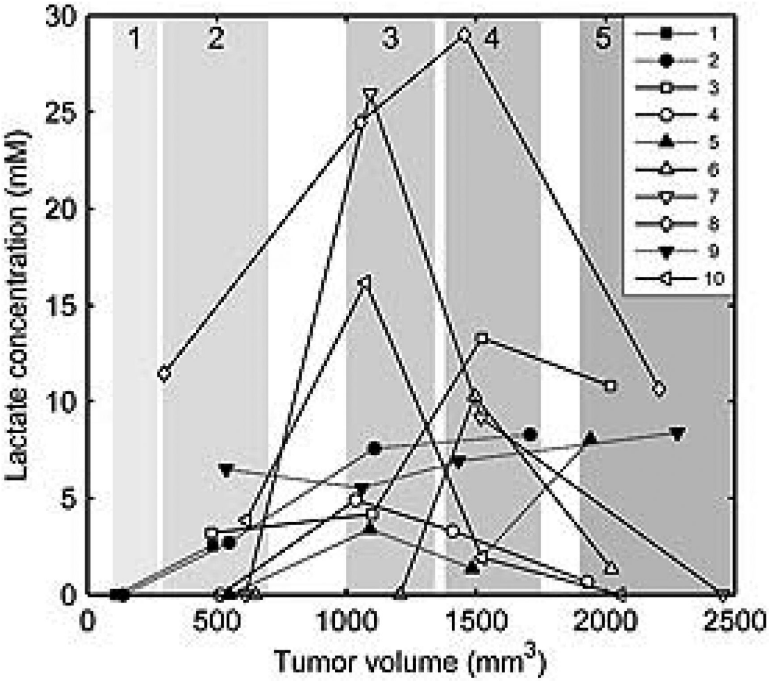

**Figure 2.**

Lactate concentration versus volume dependence in R3327-AT tumors. In rats 3, 4, 6, 7, 8 and 10 (open symbols) the lactate concentration reached a maximum at the tumor volume of 1000–1500 mm$^3$, while in rats 1, 2, 5 and 9 (filled symbols) the lactate either increased or increased and reached a plateau in this volume interval. Shaded areas indicate ranges of volume Groups 1–5.

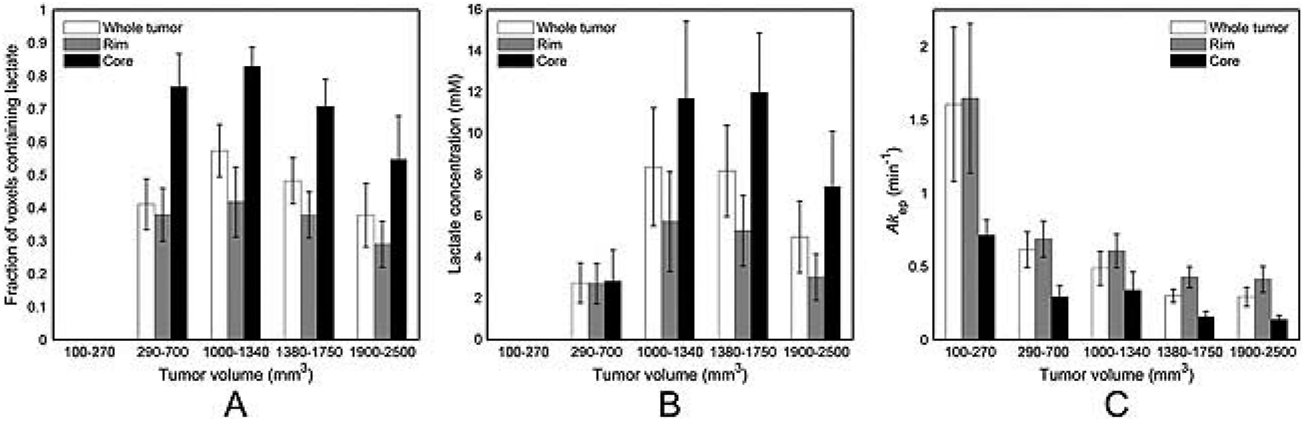

**Figure 3.**

Lactate concentration and $Ak_{ep}$ in R3327-AT tumors. The fraction of voxels in which lactate was detected (A) increased from zero for the Group 1 (100–270 mm$^3$) to 57% for Group 3 (1000–1340 mm$^3$) and declined for Groups 4 and 5. Twice as many core voxels contained lactate as the rim voxels. The mean lactate concentration (B) reached a maximum for tumors in Groups 3 and 4 for the whole tumor, rim and core and decreased at lower and higher volumes. Lactate concentration was higher in the core than in the rim. In contrast, the mean $Ak_{ep}$ values (C) decreased with volume and were higher in the rim than in the core at all volumes. Error bars are standard error of the mean.

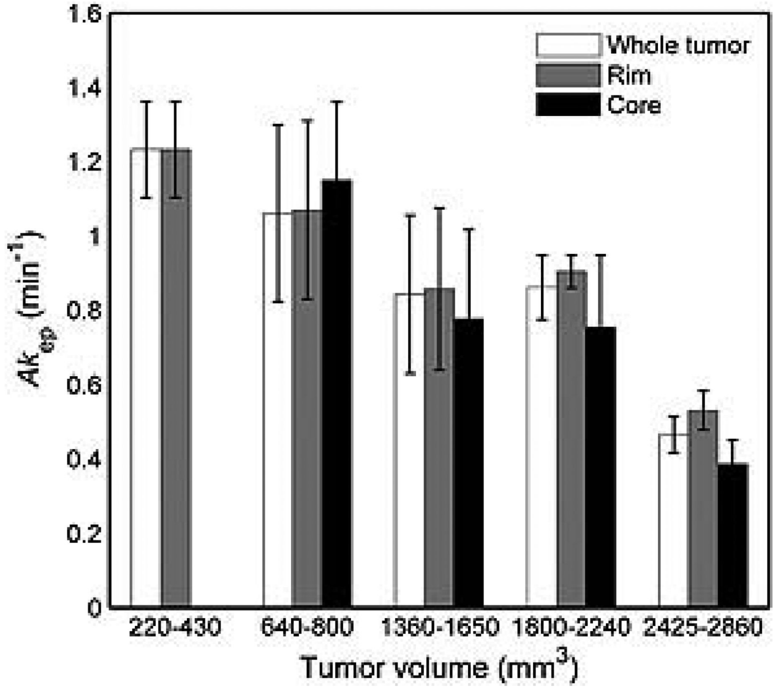

**Figure 4.**

The $Ak_{ep}$ values in Dunning H tumors decrease with increasing volume and are significantly lower in the tumor core than in the tumor rim. In Group 1 (220–430 mm$^3$) core voxels could not be identified.

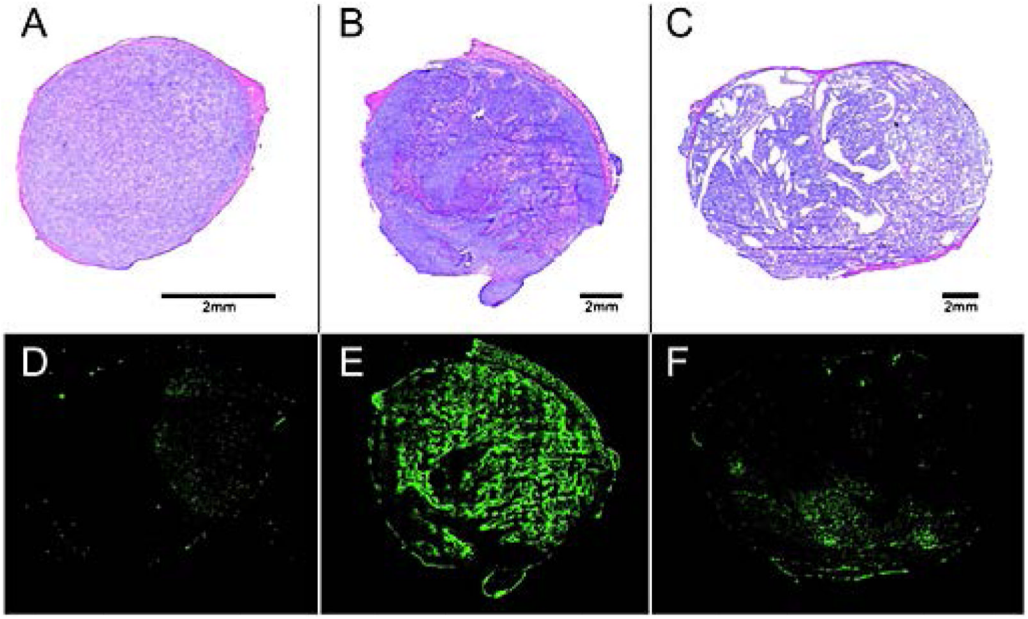

**Figure 5.**

Histology and immunohistochemistry of AT and H tumors. In AT tumors, necrosis was found even in small tumors, such as the tumor with V = 118 mm$^3$ (A) for, and increased with tumor volume (V = 2207 mm$^3$) (B). Pimonidazole-positive area also increased with tumor volume of AT tumors (D, E). In contrast, in Dunning H tumors no necrosis was observed even in large tumors (V = 1949 mm$^3$) (C) and only minimal pimonidazole activity was found (F).

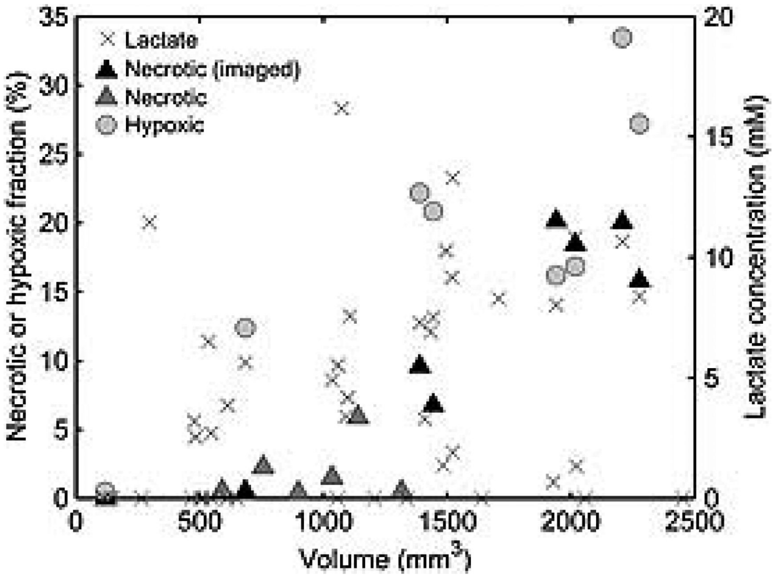

**Figure 6.**

Necrotic and hypoxic (pimonidazole-positive) fractional areas in AT tumors. Necrotic fraction was measured in tumors that were studied by MRSI and histology (n = 8, black triangles) and by histology alone (n = 6, gray triangles). Hypoxic fraction was determined for imaged tumors (n = 8, light gray circles). Both necrotic and hypoxic fractions increase with increasing volume. Lactate (crosses) is detected in tumors across the entire volume range, including tumors smaller than 1000 mm$^3$, where necrotic fraction is low (below 3%). This indicates that lactate is partly produced by the non-necrotic tumor tissue.

## Table 1

Dunning R3327-AT tumor parameters derived from lactate MRSI and DCE-MRI.

| | **Group**<br>**Volume range, mm$^3$** | | | | |
|---|---|---|---|---|---|
| **Parameter** | **1 100–270** | **2 290–700** | **3 1000–1340** | **4 1380–1750** | **5 1900–2500** |
| Lactate, mM | | | | | |
| Whole tumor | 0 | 2.8 ± 1.0 | 8.4 ± 2.9 | 8.2 ± 2.2 | 5.0 ± 1.7 |
| Rim | 0 | 2.7 ± 1.0 | 5.7 ± 2.4 | 5.3 ± 1.7 | 3.0 ± 1.1 |
| Core | 0 | 2.8 ± 1.5 | 12.0 ± 3.7 | 12.0 ± 2. 9 | 7.4 ± 2.7 |
| $Ak_{ep}$, min$^{-1}$ | | | | | |
| Whole tumor | 1.6 ± 0.5 | 0.6 ± 0.1 | 0.5 ± 0.1 | 0.3 ± 0.1 | 0.3 ± 0.1 |
| Rim | 1.7 ± 0.5 | 0.7 ± 0.1 | 0.6 ± 0.1 | 0.4 ± 0.1 | 0.4 ± 0.1 |
| Core | 0.7 ± 0.1 | 0.3 ± 0.1 | 0.3 ± 0.1 | 0.2 ± 0.0 | 0.1 ± 0.0 |

Data are mean ± standard error of the mean.

Zero entries indicate non-detectable lactate levels.

## Table 2

Dunning H tumor parameters derived from DCE-MRI. Lactate was not detected.

| | Group<br>Volume range, $mm^3$ | | | | |
|---|---|---|---|---|---|
| **Parameter** | **1 220–430** | **2 640–800** | **3 1360–1650** | **4 1800–2240** | **5 2425–2900** |
| $Ak_{ep}$, $min^{-1}$ | | | | | |
| Whole tumor | 1.2 ± 0.1 | 1.1 ± 0.2 | 0.8 ± 0.2 | 0.9 ± 0.1 | 0.5 ± 0.1 |
| Rim | 1.2 ± 0.1 | 1.1 ± 0.2 | 0.9 ± 0.2 | 0.9 ± 0.0 | 0.5 ± 0.1 |
| Core | 0[*] | 1.2 ± 0.2 | 0.8 ± 0.2 | 0.8 ± 0.2 | 0.4 ± 0.1 |

$Ak_{ep}$ values are mean ± standard error of the mean.

[*] Core voxels could not be identified in Group 1 tumors